Forschungszentrum Karlsruhe
Technik und Umwelt

Wissenschaftliche Berichte
FZKA 5595

Neutrino Flux Calculations for the KARMEN Detector at the ISIS Spallation Neutron Facility

R. L. Burman, A. C. Dodd, P. Plischke
Institut für Kernphysik

Juli 1995

Forschungszentrum Karlsruhe
Technik und Umwelt

Wissenschaftliche Berichte
FZKA 5595

Neutrino Flux Calculations for the KARMEN Detector at the ISIS Spallation Neutron Facility

R. L. Burman*, A. C. Dodd[1] and P. Plischke
Institut für Kernphysik

[1] *University of Guelph, Ontario, Canada, N1G 2W1*
* *Permanent address: P-Division, Los Alamos National Laboratory, Los Alamos, New Mexico 87545, USA.*

Forschungszentrum Karlsruhe GmbH, Karlsruhe
1995

Als Manuskript gedruckt

Forschungszentrum Karlsruhe GmbH
Postfach 3640, 76021 Karlsruhe

ISSN 0947-8620

Abstract

The neutrino flux produced by the spallation neutron source ISIS at the position of the KARMEN neutrino experiment is calculated to an accuracy of 6.7%. Contributions from the spallation and μSR targets to the ν_μ, ν_e, and $\bar{\nu}_\mu$ fluxes, due to π^+ and μ^+ decay at rest, are evaluated. Results are presented in terms of neutrinos per proton for incident proton beams of 750 and 800 MeV. The contamination of $\bar{\nu}_e$, from the π^- decay-in-flight and μ^- decay-at-rest chain, is found to be 0.06% with an accuracy of 12%.

Berechnung der Neutrinoflüsse für den KARMEN Detektor an der ISIS Spallationsneutronenquelle

Zusammenfassung

Der Fluß von Neutrinos von der Spallationsneutronenquelle ISIS am Ort des KARMEN Neutrino-Experiments wird berechnet mit einer Genauigkeit von 6.7%. Beiträge des Spallations- und des μSR- Targets zu den Flüssen von ν_μ, ν_e und $\overline{\nu}_\mu$ aus dem π^+ und μ^+ Zerfall in Ruhe werden ausgewertet. Die Ergebnisse werden dargestellt als Neutrinos pro Proton für Protonenenergien von 750 und 800 MeV. Der störende Anteil an $\bar{\nu}_e$ aus dem π^- Zerfall im Fluge und anschließendem μ^- Zerfall in Ruhe wird zu 0.06% bestimmt mit einer Genauigkeit von 12%.

Contents

1 Introduction

The ISIS facility at the Rutherford Appleton Laboratory in Oxfordshire, UK, is based on an 800 MeV rapid-cycling (50 Hz) proton synchrotron with a design beam intensity of 200 μA. The protons are dumped in a massive tantalum or uranium target, producing neutrons from spallation and fission processes [1]. These are used to provide an intense pulsed neutron source suitable for condensed matter studies. A thin carbon target, inserted upstream of the neutron spallation source, produces a polarized muon beam for muon-spin-resonance (μSR) studies. In addition, the facility serves as a high-intensity pulsed neutrino source for the KARMEN neutrino experiment[2], operated by a collaboration of the Forschungszentrum Karlsruhe, University of Karlsruhe, University of Bonn, University Erlangen-Nürnberg, Rutherford Appleton Laboratory, Queen Mary and Westfield College, London and Oxford University.

About 15% of the incident protons produce a pion in interactions within the spallation target. The charged pions produced in the tantalum or uranium target stop very quickly (< 1 ns) because of their relatively low energies ($\sim$ 100 MeV), and because of the high stopping power of the target material, so that most of the π^+ decay at rest. Because the pion has spin 0, both the μ^+ and the associated ν_μ are emitted isotropically. The π^+ decay at rest is followed by the μ^+ decay within 0.2 g/cm^2 of the point at which the π^+ stopped, as the muon kinetic energy is 4.1 MeV. Again, because of the isotropic distribution of muon momenta, the $\overline{\nu}_\mu$ and ν_e fluxes are isotropic. The majority of these pions decay in the immediate vicinity of their production point, and thus the ISIS spallation facility represents an extremely intense, approximately point-like, source[3] of neutrinos for nuclear and particle physics studies. The π^- produced which stop are all absorbed by nuclei. No neutrinos are emitted in this process. It is the 1% of produced π^- that decay in flight, and the fraction of resulting μ^- that decay at rest rather than capture, that lead to production of a $\overline{\nu}_e$ background.

A Monte Carlo code for pion production and pion and muon tracking has previously been developed[4] for the simulation of neutrinos from π^+ and μ^+ decay at rest; the code has been used for neutrino experiments at ISIS and at the Los Alamos Meson Physics Facility (LAMPF). This paper describes the addition to that code of the production and tracking of negative pions, and of the application of the code to the neutrino fluxes from the ISIS facility. The contamination of the neutrino flavour and energy distributions by the production of π^- and their eventual $\overline{\nu}_e$ decay product is considered in detail because it limits the sensitivity of neutrino oscillation searches at ISIS. The time-structure of the ISIS proton beam, and the spallation and μSR targets and their modelling for the Monte Carlo code, are briefly described in Sec. 2. The neutrino production Monte Carlo code and its normalization are described in Sec. 3. The extension of the code to include π^- production and decay in flight, and the tracking of μ^- until eventual absorption or decay at rest, is discussed in Sec. 4. Calculated neutrino fluxes from the spallation target and from the μSR target, and the background flux of $\overline{\nu}_e$ neutrinos are displayed in Sec. 5. The uncertainties in these neutrino fluxes are discussed in Sec. 6.

2 ISIS neutrino source

2.1 Time structure

It is the time structure in the ISIS proton beam that enables the physics of the KARMEN project to be separated into that initiated by ν_μ neutrinos or by ν_e and $\overline{\nu}_\mu$ neutrinos. The proton beam consists of a pair of 100 ns wide pulses separated in time by 330 ns, within a 20 ms beam cycle.

The ν_μ neutrinos, with an energy of 29.8 MeV from the two-body π^+ decay at rest, have a time structure characteristic of the 26 ns pion mean life; the ν_e and $\overline{\nu}_\mu$ neutrinos, with the 0-53 MeV Michel spectral shapes from the three-body μ^+ decay, have the time structure of the 2.20 μs μ^+ mean life. This allows the separation (by timing) of the neutrinos produced from the pion decay, and from the subsequent muon decay.

2.2 ISIS spallation target

Fig. 1 shows an overview of the ISIS spallation target and its surroundings. The 800 MeV proton beam passes through a water cooled inconel beam window, then a helium filled void. It is stopped in a target, designed to produce spallation neutrons, consisting of layers of thin disks of tantalum or of depleted uranium clad in zircalloy. Each disk has a diameter of 90 mm, and as shown in fig. 2a is held in a square stainless steel retaining plate; the spaces between and surrounding the disks are filled with rapidly flowing heavy water as a coolant. The proton beam spatial distribution[5] is a parabola 70 mm across, so that it is entirely contained within the area of the uranium disks.

This assembly of plates is held within a stainless steel pressure vessel, containing manifolds for heavy water coolant. The geometry of the pressure vessel was modelled as shown in figs. 2a and 2b, with three layers of steel and three layers of water. The total thickness of steel reproduces the volume of steel in the pressure vessel (excluding the top and bottom plates which could be modelled more exactly). A similar procedure was used for the water layers within the pressure vessel.

Surrounding the pressure vessel is the neutron reflector system, a vessel containing beryllium rods immersed in heavy water, and neutron moderators. This system was modelled as a cylinder of beryllium with the density reduced by 10% to roughly simulate the presence of the heavy water. Between the beam windows and the reflector vessel, there is a beam halo monitor which is mounted on an aluminium flange. This was modelled as a circular ring 5cm thick, and was included because of its effect on the absorption of pions produced in the beam window.

2.3 ISIS μSR target

Between 0.5% and 2.0% of the proton beam interacts in the μSR facility[6] pyrolytic graphite target located 21.5m upstream of the main ISIS spallation target. The distance from the KARMEN detector to the μSR target is 27.7m, further than the distance,

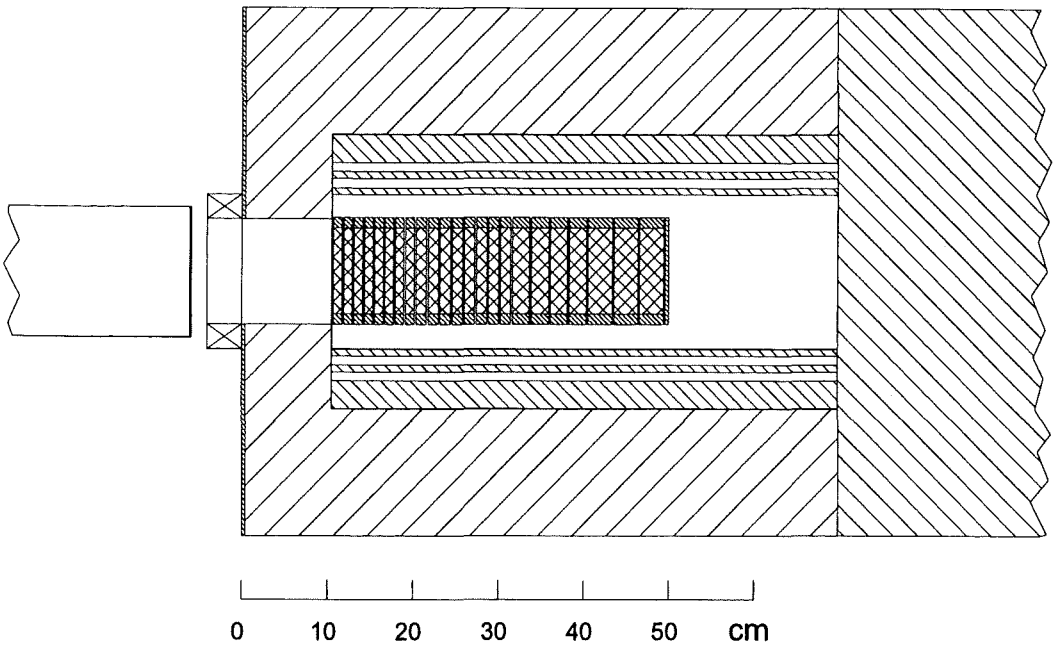

Figure 1: Computer model of the ISIS spallation target assembly with the proton beam incident from the left. Shown are the proton beam pipe, exit vacuum window, entrance collimator, and target structure.

17.5m, to the main ISIS target. However, because the target is made of carbon, which is a better material for producing π^+ than uranium (for a given thickness in g/cm^2), the pion production in the μSR target is as much as 6% of the pion production within the main target. Thus it is necessary to model this source of neutrinos in detail.

Pions produced within the graphite target will usually escape, and mostly be stopped or absorbed, within the steel shielding around it. This has been modelled with the Monte Carlo code. A second source of pions is due to protons that scatter at small angles and hit the collimators and beam pipe downstream of the μSR target. These effects have not been modelled directly, as there are many magnets in the proton beam line and the Monte Carlo does not include the effect of magnetic fields in its handling of the proton transport. Beam transport calculations have shown that (for the 5mm target) 0.56% and 0.24% of the beam hit the two copper collimators located downstream of the μSR target, and 0.45% are lost in the stainless steel proton beam pipe further downstream. Thus there are three sources of neutrinos associated with the μSR target: the target and its shielding; the copper collimators; and the proton beam pipe.

The first source is modelled as a pyrolytic graphite disc 25mm in radius, centered within a rectangular cavity in the steel shielding that is 25cm by 25 cm in the horizontal plane, and extends 56cm upwards and 35cm downwards, with outlets for the proton beam fore and aft, and to one side for the Muon channel. The cavity walls are modelled

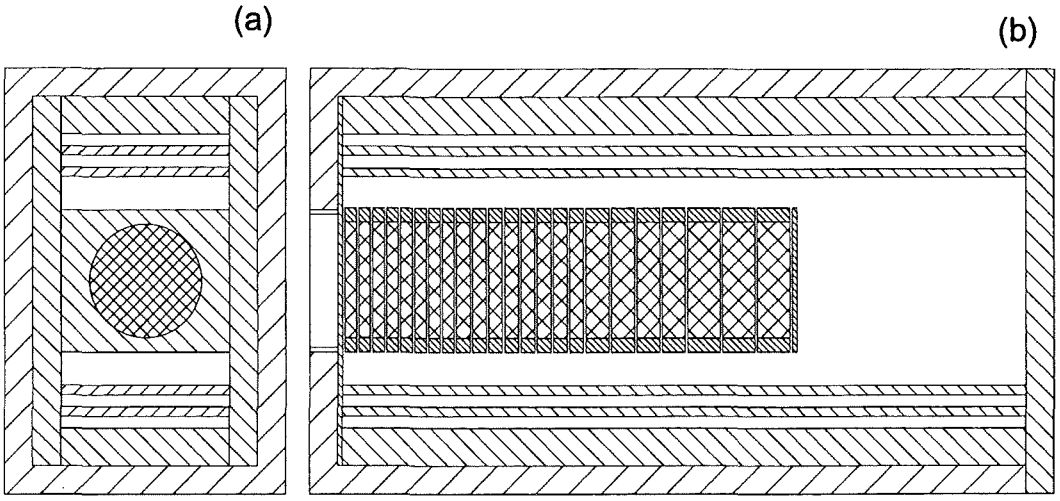

Figure 2: Computer model of the ISIS spallation target, with the heavy-metal target shown in cross-hatching. (a) Frontview of the uranium or tantalum plate structure; (b) topview of the plate structure within the pressure vessel.

as thick iron, hence most of the pions decay within the shielding around the target. The proton beam is 2.0 cm wide at the μSR target.

Actual μSR target thicknesses used were 2.5, 5.0, and 10.0 mm; but as the pyrolytic graphite target is inclined at 45^0, the effective target thicknesses were 3.5, 7.1, and 14.1 mm, with a density of 2.23 gm cm^3. In general, all the effects of the μSR target are found to scale linearly with thickness.

The effect of the collimators has been modelled by assuming that any protons hitting them are stopped within them; this is reasonable since this is one of their design objectives. The neutrino production is then estimated using a pure copper beam dump as the geometry input for the Monte Carlo, and then scaling the results by the fraction of the proton beam that strikes the collimators. The beam pipe wall is only 2.03mm in thickness, but it is surrounded by quadrupole magnets for much of its length downstream of the copper collimators. The effect of the proton beam that is lost in the beam pipe is modelled by assuming that the protons stop in a iron beam dump and represent a line source of neutrinos. This is a reasonable approximation because the copper collimators restrict the proton angles to within 2° of the beam axis. Thus protons which do not stop within the beam pipe will reach the quadrupole magnets and stop in these.

3 Neutrino flux Monte Carlo code and normalization

A Monte Carlo code has been developed to calculate neutrino fluxes from π^+ and μ^+ decay at rest and decay in flight, for spallation targets or beam stop facilities at medium-energy proton accelerators. Since the code[4] has been described before in detail, we mention here only its main features. It is designed to calculate the neutrino production by medium energy protons incident on thick targets. It allows the user to specify the target geometry and composition, as well as the proton beam energy. The geometry package has been taken from the standard neutron transport code MCNP[7]; the input geometry specification is identical to that used for MCNP. Proton reaction cross sections, pion production and absorption cross sections, and particle transport are used to calculate the neutrino fluxes from the decays of π^+ and μ^+. The proton beam is transported, with energy loss, through the target geometry. At a Monte Carlo chosen proton interaction point, pions, weighted by the production cross sections, are selected with initial energy and angle according to measured cross sections. As the pions are tracked through the target geometry they are allowed to inelastically scatter, to multiple-Coulomb-scatter, to be absorbed, or to decay.

Absolute normalization was provided by measurements[8] made on an instrumented mockup of a simplified beam stop; the event-by-event production of pions, followed by signals from pion and muon decay, was used to infer the rate of stopped π^+ production per incident proton. Data on the stopped π^+ rate were taken for beam stops composed of copper, water + copper, and lead for proton energies of 716, 766, and 797 MeV. The output of the code was then compared to the data[4]; it was found that the distribution of stopped π^+ production *versus* depth in the target fell faster than the calculation. To correctly model the measured stopped π^+ longitudinal distribution, it was necessary to normalize the code by a 10% increase in the overall proton reaction cross section, and to retain the agreement in the absolute pion production rate by a similar increase in the pion production cross section. As 10% relative uncertainties and 10% normalization uncertainties in these measured cross sections are typical, this correction is quite reasonable. It should be noted that these effects changed the pion production spatial distribution but essentially **canceled** in the pion production rate.

For calculation of neutrino fluxes from the ISIS facility, the proton beam is assumed to be perfectly aligned along one axis. Parameters for the parabolic beam shape used in the code are those measured for the ISIS proton beam[5]. The dependence of the neutrino production upon atomic number, proton number and neutron number (A, Z, N) comes from the dependence of the pion production and absorption on A and Z. For heavier elements ($Z > 12$), the pion production per nucleus scales as $Z^{1/3}$ for π^+ production and $N^{2/3}$ for π^- production, whereas the absorption (including charge exchange as very few π^0 decays produce neutrinos) scales roughly as $A^{3/4}$ [9]. This slow dependence of the neutrino production on A and Z allows good interpolation to materials other than those defined in the parameterizations within the code.

4 π^- production and π^- and μ^- tracking

Because of the virtual absence of the π^- decay chain, the KARMEN neutrino oscillation experiment is designed to look for the appearance of $\overline{\nu}_e$ neutrinos which should not be present in a beam stop neutrino source. Any such neutrinos that are present are a background for neutrino oscillations searches in the $\overline{\nu}_\mu \rightarrow \overline{\nu}_e$ channel; their number can only be obtained by an absolute calculation starting with π^-decay in flight. The calculation with the code of π^+ and μ^+ decay at rest has been normalized, as explained above, to a mock beam-stop experiment. Therefore, for the $\overline{\nu}_e$ flux it is important to be able to both (a) calculate the μ^- decay at rest with the detailed Monte Carlo code, and (b) make a reliable estimate of the ν flux from μ^- decay at rest with which to check the detailed Monte Carlo code.

The time taken for the formation and de-excitation of the pionic atom is about 10^{-13}s. All stopped π^- may be assumed to be captured into pionic atoms. The rate at which the pions are absorbed by nuclei ($> 10^{14}s^{-1}$) is very much larger than the pion decay rate ($< 4 \times 10^7 s^{-1}$). Therefore the possibility of the π^- decaying after it has stopped may be neglected, and the principal source of contamination is from the approximately 1% of the π^- that decay in flight. The μ^- from the decay in flight are tracked until they stop in a particular material; the fraction that leads to decay at rest rather than to absorbtion is calculated and is used to predict the $\overline{\nu}_e$ background.

4.1 Estimate of $\overline{\nu}_e$ flux

The number of π^- decays in flight can be estimated from the number of π^+ decays in flight (given by the code) and the ratio of π^-/π^+ production cross sections for a given material. It is the decay of the μ^- which produces the $\bar{\nu}_e$, and is the source of contamination. The time taken for the muons produced in the ISIS spallation target to stop in condensed materials is similar to that taken by pions to stop, < 1 ns, which is much shorter than the muon lifetime of 2.2 μs. Therefore the possibility of the μ^- decaying in the slowing down time may be safely neglected. After it has been degraded to $\sim$ keV energies, the μ^- will be captured into muonic atoms, where the usual muon decay has to compete with nuclear muon capture, which only produces muon neutrinos. This capture probability increases strongly with atomic charge Z, and so the stopping positions of the μ^+ have been used to simulate that of the μ^-.

We begin the estimation of the $\overline{\nu}_e$ flux, from a uranium spallation target, by noting that the fraction of π^+ that decay in flight is only 1.2% of the total number of π^+ decays because of the high stopping power of the uranium target. The π^-/π^+ production ratio is known to be 0.56 ± 0.06, for thorium at 730 MeV [10], so the fraction of π^- decays in flight is $< 0.65\%$. Since the π^- momenta are lower than the π^+ momenta (by ~ 40 %) they (a) stop more quickly, allowing less time for them to decay in flight, and (b) produce lower-energy muons that are less likely to stop outside of the high-Z target. Thus the contamination estimated on the basis of the π^+ decays in flight is, in condensed media,

Table 1: Estimate of $\bar{\nu}_e$ contamination, per 10^4 incident protons, at 800 MeV.

Component	μ^+ stops	μ^- decay probability	$\bar{\nu}_e$ production
Uranium	0.890	0.035	0.016
Water	0.058	0.740	0.021
Copper	0.031	0.070	0.001
Iron	4.370	0.090	0.155
Beryllium	1.010	0.950	0.379
Total			0.572

an overestimate.

From the spallation target geometry and the distribution of stopping μ^-, we expect that most of the free μ^- decays will occur when the μ^- penetrate the pressure vessel and stop in the beryllium/heavy water mixture of the reflector system, where the probability for their free decay is very high ($\simeq 95\%$)

The contamination can now be computed using a two dimensional histogram of materials in which the muons stop against the materials from which the π^+ decays in flight originate. The contents of each cell is then weighted by the appropriate π^-/π^+ production ratio, and the probability of free μ^- decay for the μ stopping material. Table 1 shows, for each of the materials within the ISIS spallation target, the number of μ^+ from π^+ decays in flight that stop within the material, the probability of free μ^- decay in these materials[11], and the resulting $\bar{\nu}_e$ production, per 10^4 incident protons. The estimated value for the uranium target, 0.57×10^{-4}, is for the reasons discussed above an upper limit. These results will be compared with the output of the KARMEN Monte Carlo code in Sec. 5.4 .

Most of the contamination from π^- decays in flight, as listed in Table 1, are due to π^- produced in the inconel beam window and in the uranium, with the μ^- decays occuring in the beryllium/D_2O mixture in the reflector system. The third largest source is due to π^- decay in flight in the relatively large void spaces around the beam window, with the μ^- stopping in the surrounding iron shielding. The estimated $\bar{\nu}_e$ flux from the muon target, not included in Table 1, is less than 10% of the total from the spallation target, and will be neglected.

4.2 Modelling of π^-production

Two precise sets of cross section data on inclusive π^- production exist: at incident proton energies of 730 MeV[10] and 585 MeV[12]. These are thin-target doubly-differential cross sections, in pion kinetic energy (T_π) and angle (θ), for a variety of

materials spanning the periodic table. As the pion production cross sections will be

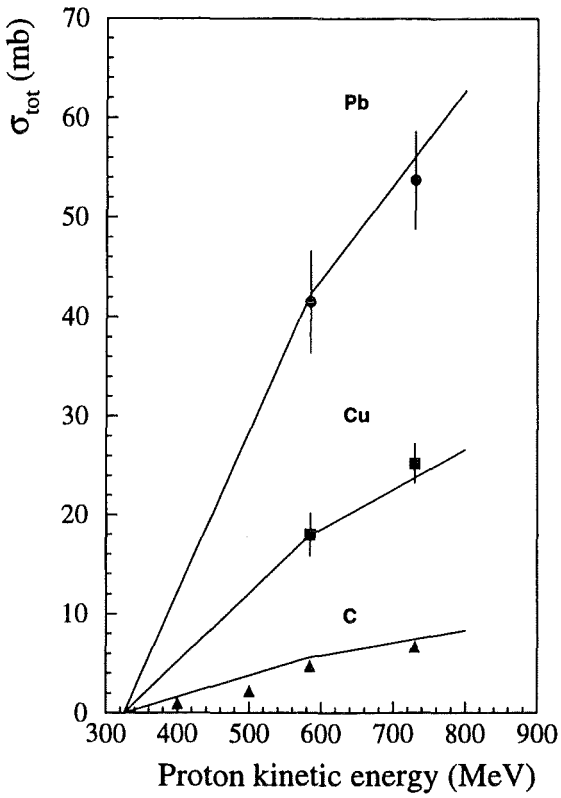

Figure 3: The total π^- production cross sections, σ_π, for carbon, copper and lead as functions of the proton energy T_π. A simple piece-wise linear energy dependence is assumed, with σ_π decreasing to zero at 325 MeV.

used both for interpolation (in pion energy and angle) and for extrapolation (in proton energy and in target material), we want simple algorithmic forms, with smoothly varying parameters, for the cross sections. A procedure similar to that used for the modelling of π^+ production[4, 13] is followed. The dependence upon π^- kinetic energy T_π is conveniently defined, for a given material Z and proton kinetic energy T_p, in terms of a sum of Gaussian forms:

$$\frac{d^2\sigma}{d\Omega_\pi dT_\pi} = \left[A_1 e^{-\left(\frac{\overline{T}-T_\pi}{\sqrt{2}\sigma_1}\right)^2} + A_2 e^{-\left(\frac{T_\pi}{\sqrt{2}\sigma_2}\right)^2} \right] \times \left(1 + e^{\frac{T_\pi - T_F}{B}}\right)^{-1} . \qquad (1)$$

The functional dependence on T_π is simple, it appears only in the exponents of the Gaussians and in the high-energy cut-off factor. Use of a Gaussian function to approximate[14] the energy dependence is strongly suggested by the measured data on pion production;

see figs. 4-6. In the data for π^- production, a need for a second Gaussian shape in eq. (1), centered at $T_\pi = 0.0$, is apparent for atomic number $A > 24$, as is evident in fig. 5. A high-energy cut-off factor, the last term in eq. (1), is employed to produce a smoothed form of energy conservation, $T_F = T_p - 140$ MeV $- 2$B, where the sharpness of the cut-off is determined by the parameter B, set to 25 MeV. The parameters A_i, $\overline{T}$ and σ_i were obtained by fitting the data in references [10, 12] using standard minimization techniques. Simple piecewise-continuous analytical forms suffice for the dependence of these parameters upon Z, T_p, and θ; the detailed functional forms are given in appendix A. The total cross section,

$$\sigma_\pi = \int\int \frac{d^2\sigma}{d\Omega_\pi dT_\pi} dT_\pi d\Omega_\pi \ , \tag{2}$$

obtained by integration of the parameterization of the differential cross section, is normalized to experiments at proton energies of 730 and 585 MeV. Measurements[10, 12] of the total cross sections at 730 and 585 MeV are fit well by an $N^{2/3}$ dependence:

$$\begin{aligned} \sigma_\pi(730 \text{ MeV}) &= 2.24\ N^{2/3}, \\ \sigma_\pi(585 \text{ MeV}) &= 1.69\ N^{2/3} \end{aligned} \tag{3}$$

where $N = A - Z$ is the neutron number of the target nucleus. We assume the total cross section to be a linear function of T_p, where we interpolate between measured values at 730 and 585 MeV. Above 730 MeV the total cross section is extrapolated linearly with the same slope, while below 585 MeV it decreases linearly to zero at T_p= 325 MeV. This dependence upon T_p is illustrated in fig. 3 for carbon, copper and lead.

Our parameterization of pion production is compared to the data of references [10, 12] in figs. 4-6. The data at T_p= 730MeV has been relied on most heavily because it is the most extensive; however, the parameterization reproduces all the data, at both energies, quite well. The second Gaussian energy term, in square brackets in eq. (1), is non-zero (coefficient $A_2(\theta) > 0.0$) only for $A > 24$, and therefore shows up in the calculated cross sections for copper and lead, but not for carbon. The total cross section, obtained by integration of the parameterization of the differential cross section, reproduces the published cross sections to $\sim$ 10%. On the whole, this representation of negative pion production is quite convincing and predicts the cross sections for all materials, for proton energies below 800 MeV, and for all pion production angles and energies. In the implementation of the Monte Carlo code, the parameterization of eq. (1) is used to form two-dimensional (pion energy and angle) integral probability tables for the materials contained in the geometrical simulation.

4.3 π^- and μ^- tracking

Of the pions produced from interactions of the proton beam in the spallation target, about 20% are π^-. Details of the simulation of π^+ tracking are given in Ref. [4], so we shall here concentrate upon the differences between the handling of π^- and π^+. At

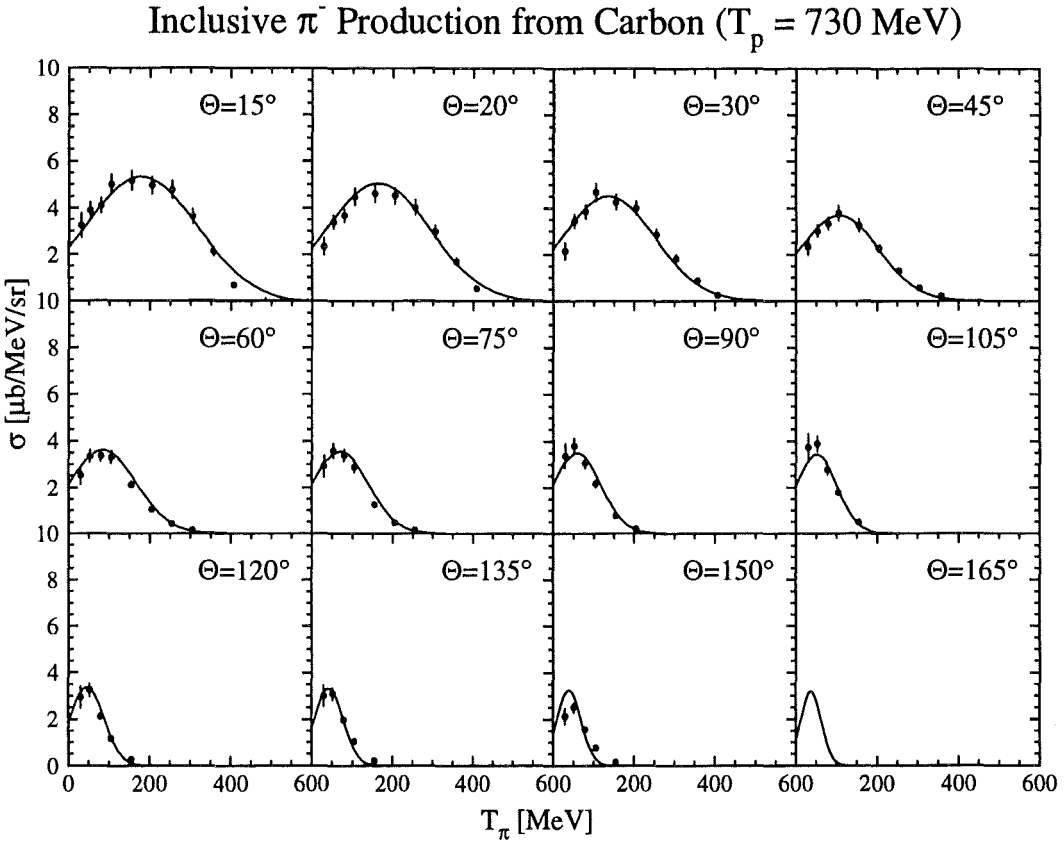

Figure 4: Comparison of the calculated π^- production doubly-differential cross section (solid line) for carbon at 730 MeV proton energy with the data of ref.[10]. The parameterization is that of eq. (1).

each proton interaction in the spallation target a π^- with the appropriate energy and direction is produced with a weight given by the ratio σ_π/σ_I of the π^- production to proton reaction cross sections. The overall normalization of π^- production is adjusted by the same factors as for π^+ production, as described in Sec. 3. In the same manner as for π^+ transport, the π^- are tracked through the geometry by the Monte Carlo code, with tests at each step for decay in flight, inelastic reactions, multiple Coulomb scattering, and absorption. Energy loss by ionization limits the π^- flight time to a few nsec; any π^- that survive to come to rest are assumed to be absorbed. Therefore the only mechanism for producing μ^- is the 1% of the π^- that decay in flight. The tracking of the pions proceeds through computation, at each step, of the absorption and inelastic cross sections, σ_{abs} and $\sigma_{inelastic}$, and their sum, the reaction cross section σ_{reac}. For π^-, the $\sigma_{inelastic}$ has the same value as for π^+, while σ_{abs} is increased by giving the π^- a

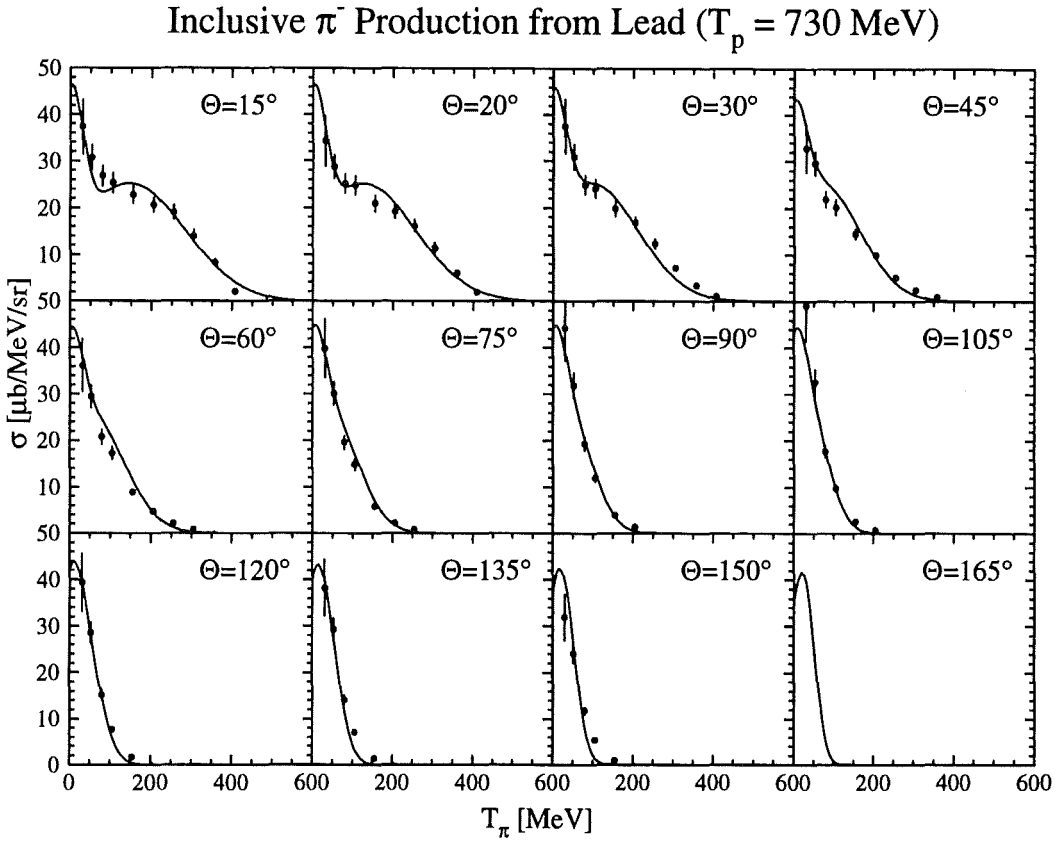

Figure 5: Comparison of the calculated π^- production doubly-differential cross section (solid line) for lead at 730 MeV proton energy with the data of ref.[10]. The parameterization is that of eq. (1).

larger effective kinetic energy from the Coulomb attraction[15] leading to

$$\begin{aligned} \sigma_{abs}(\pi^-) &= \left(\frac{1+C}{1-C}\right)\sigma_{abs}(\pi^+), \\ C(T_{\pi^-}) &= Z\alpha/RT_{\pi^-}. \end{aligned} \tag{4}$$

The nuclear radius is taken to be $R = 1.2A^{1/3}$ and α is the fine structure constant. With this adjustment in the absorption cross section, the π^- reaction cross section is now

$$\sigma_{reac}(\pi^-) = \sigma_{abs}(\pi^-) + \sigma_{inelastic} \tag{5}$$

The decay in flight of π^-, however, leads to another sequence of events. An energy and angle are chosen for the μ^- and $\overline{\nu}_\mu$, and the μ^- is tracked through the spallation target geometry, losing energy via ionization losses, until it stops in a particular material. The fraction that leads to decay at rest rather than to absorbtion is then calculated.

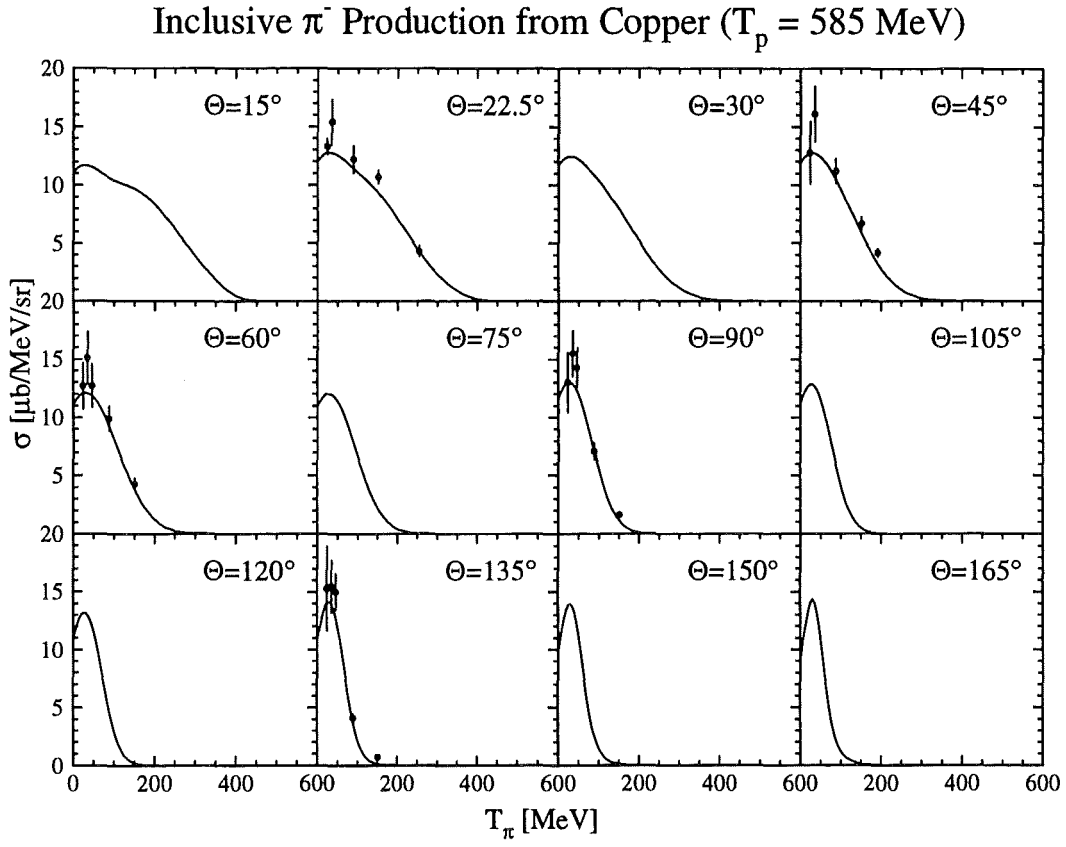

Figure 6: Comparison of the calculated π^- production doubly-differential cross section (solid line) for copper at 585 MeV proton energy with the data of ref.[12]. The parameterization is that of eq. (1).

In order to improve the program efficiency, a choice of μ^- and $\overline{\nu}_\mu$ energies and angles is made many times (typically 100) at each decay-in-flight π^- position, and the tracked muons appropriately weighted.

5 Calculated neutrino fluxes

5.1 Relative acceptance

The acceptance of the KARMEN detector for neutrinos from stopped pion and muon decay, for the various sources, is a product of two factors: (1) the solid angle subtended at the source, and (2) the detection efficiency, which is proportional to the detector thickness seen by the neutrino source. This has been calculated[16] for each of the neutrino sources; Table 2 shows the distances involved and the relative acceptances.

Table 2: Neutrino production per 10^4 incident protons and acceptances at the centre of the KARMEN detector. The ISIS target is uranium; the μSR target is 5mm graphite.

Source	Distance	Acceptance	Neutrino Production	
			750 MeV	800 MeV
	(meters)	(arb. units)	(per 10^4 protons)	
ISIS Target	17.5	1	345.	401.
μSR Target	27.7	0.375	19.2	21.5
Collimator 1	26.9	0.396	3.1	3.6
Collimator 2	26.0	0.422	1.3	1.6
Beam Line		0.660	2.6	3.1

The calculations of neutrino production are explained in the following section, but we should note here that the total contribution from the μSR target, the last four lines of Table 2, is $\sim$ 3% of that from the ISIS target. In this calculation, neutrino fluxes into the KARMEN detector are computed by multiplying the production rate by the relative acceptance. In the remainder of the paper we will add together these neutrino contributions (μSR target, collimators 1 and 2, and beam line) under the designation "μSR target".

5.2 Neutrino production from π^+ decay at rest

Input to the Monte Carlo code was provided by the ISIS spallation target model described in detail in Sec. 2.2 . For this geometry, all of the pion production and over 75% of the pion decays occur within the spallation target plate assembly. Only the fraction of pions absorbed outside the plate assembly ($\sim$ 6%) is sensitive to the modelling of the pressure vessel. This region is, however, of more importance to the calculations of neutrino backgrounds from the π^- to μ^- decay chain.

The decay-at-rest neutrino production, for both target materials (tantalum and uranium) and for the two proton energies (750 and 800 MeV) that have characterized the Rutherford accelerator operation, is given in Table 3. Results are expressed as the number of π^+ decays at rest per incident proton for the target/beam configurations used. It is seen that, in their present design, the uranium target produces a neutrino flux about 90% of that from the tantalum target. A discussion of the $\overline{\nu}_e$ background listed in the last column of Table 3 will be given in Sec. 6. Table 4 shows the breakdown of π^+ production, decay and absorption by material type. As expected, the bulk of the pion production is in the uranium material in the spallation target stack assembly. However, appreciable numbers of π^+ travel out of the stack to stop in the steel cooling lines and pressure vessel, and in the beryllium + D_2O reflector.

Table 3: Calculated neutrino fluxes with the tantalum, uranium and μSR targets for proton beam energies of 800 and 750 MeV. Column 3 gives the neutrino production from μ^+ decay at rest in units of ν per proton, while column 4 gives the $\overline{\nu}_e$ background from μ^- decay at rest as a fraction of the number in column 3.

Spallation Target	Proton Energy (MeV)	Neutrino Flux ν_μ, ν_e, $\overline{\nu}_\mu$ (ν p^{-1})	Ratio $\overline{\nu}_e$ / ν_e (10^{-3})
Tantalum	800	0.0448	0.62
Uranium	800	0.0401	0.72
μSR	800	0.0012	0.03
Tantalum	750	0.0382	0.57
Uranium	750	0.0345	0.67
μSR	750	0.0011	0.03

5.3 Proton energy loss from the μSR target

After the proton beam passes through the μSR target, the proton kinetic energy will be reduced by up to several MeV. Over this range the dependence of the neutrino flux on the proton beam energy is nearly linear and independent of target material (tantalum or uranium). The fractional change in the flux $\phi(T_p)$ is found from calculations with the Monte Carlo code to be

$$\begin{aligned} \Delta\phi/\phi(T_p) &= (-.0028)\Delta T_p, \qquad T_p \sim 800 MeV \\ &= (-.0032)\Delta T_p, \qquad T_p \sim 750 MeV. \end{aligned} \tag{6}$$

The actual neutrino flux from the spallation facility then has a small increase from π^+ production, and a small decrease from proton energy loss, in the μSR target. Table 4 shows these effects for a 5mm pyrolytic graphite target, where the total change in the neutrino flux is typically +2%. (No change has been made for the intensity loss in the μSR target, of several per cent, because the beam intensity is measured down-stream of the μSR target.)

5.4 Neutrino background from μ^- decay at rest

Virtually all π^- that stop are absorbed, and so the possible $\overline{\nu}_e$ backgrounds are created from the approximately 1% of the π^- that decay in flight. The μ^- from the decay in flight are tracked until they stop in some particular material; the fraction that leads to decay at rest rather than to absorbtion is calculated from measured muon total absorption rates[11] and is used to predict the $\overline{\nu}_e$ background. These fluxes, as a ratio to the ν_e flux, are shown in the last column of Table 3. From the entry for a uranium target and an 800 MeV proton beam, we get 0.29×10^{-4} $\overline{\nu}_e$ per incident proton. This

Table 4: π^+ production in the ISIS uranium target per 10^4 protons incident at 800 MeV

Component	π^+ production	π^+ absorption	ν production
Uranium	395.7	96.2	266.2
Water	43.5	1.9	13.2
Copper	50.9	1.9	8.8
Iron	24.3	14.3	71.8
Zirconium	15.9	1.9	9.2
Beryllium + D_2O	0.0	5.5	29.5
Aluminium	0.0	0.7	2.3
Total	530.3	122.4	401.0

Table 5: Calculated neutrino fluxes from proton beams of 800 and 750 MeV, incident upon a 5mm μSR target in series with either a tantalum or a uranium spallation target. Neutrino flux at the KARMEN detector in units of ν per proton.

Target	T_p	Spallation Target Flux	μSR Flux	ΔT_p (MeV)	Flux loss from ΔT_p	Total Flux
Ta+μSR	800	0.0448	0.0011	2.40	0.0003	0.0456
U+μSR	800	0.0401	0.0011	2.40	0.0003	0.0409
Ta+μSR	750	0.0382	0.0010	2.45	0.0003	0.0389
U+μSR	750	0.0345	0.0010	2.45	0.0003	0.0352

number is in reasonable agreement with the upper limit 0.57×10^{-4} of Sec. 4.1, and thereby gives us increased confidence in the results of the π^- decay-in-flight parts of the Monte Carlo code.

Time structure in the ISIS proton beam, described in Sec. 2.1, enables this background to be substantially reduced. The time spectrum of $\overline{\nu}_e$ from the decay at rest of μ^- in the uranium spallation source is shown in fig. 7. Here, the double-peaked initial shape is a consequence of the proton time struture, made up of two 100 ns wide pulses separated in time by 330 ns, with a repetition rate of 50 Hz. The total $\overline{\nu}_e$ time spectrum then consists of two basic components: (1) an exponential decay in low-Z materials Be and D_2O dominated by the 2.2 μs muon mean life, and (2) the much faster exponential decay in high-Z materials Fe, U and Cu characterized by a fast absorption rate.

Because the physics of the KARMEN experiment is normally separated into that due to ν_μ interactions (from the 26 ns π^+ decay at rest), and that due to ν_e and $\overline{\nu}_\mu$ interactions (from the 2.2 μs μ^+ decay at rest), events are separated into two time groups, above

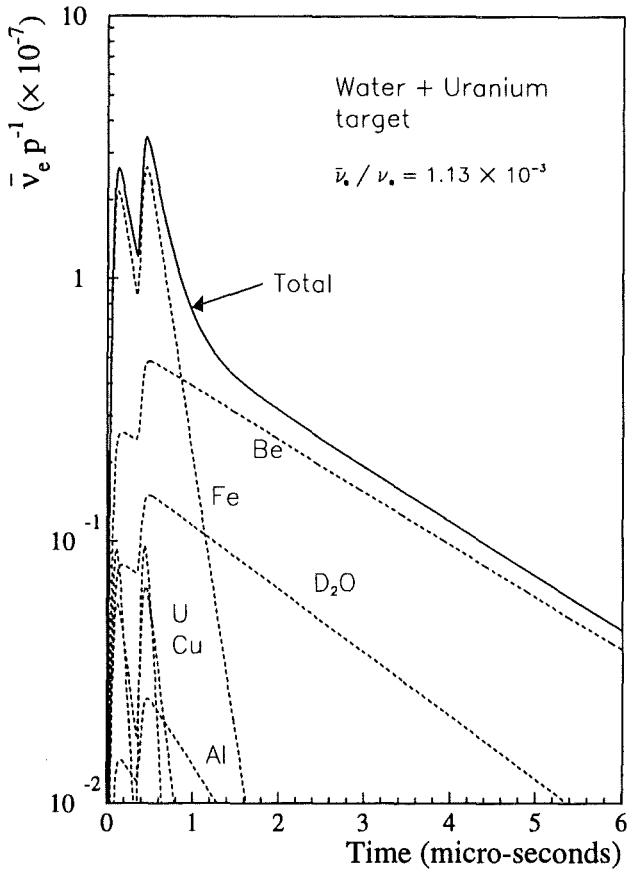

Figure 7: The time spectrum of $\overline{\nu}_e$ from the decay at rest of μ^- in the heavy water plus uranium spallation target combination. The double-peaked initial shape is due to the proton time struture, while the total $\overline{\nu}_e$ time spectrum consists of two basic components, a relatively slow decay rate in low-Z materials (Be and D_2O) and the faster decay rate in high-Z materials (Fe, U and Cu).

and below 600 ns from the start of the proton pulses. Inspection of fig. 7 shows that 65% of the $\overline{\nu}_e$ are emitted after 600 ns, compared to 85% of the $\overline{\nu}_\mu$. Thus, *e.g.*, the expected experimental background to a neutrino oscillation search for the uranium target would be reduced from 0.72×10^{-3} in the last column in Table 3 to a value $\overline{\nu}_e / \nu_e = 0.55 \times 10^{-3}$.

6 Neutrino flux uncertainty

Estimates of the flux uncertainties for the KARMEN decay-at-rest neutrino source are based upon the detailed error analysis for the decay-at-rest fluxes as discussed in ref[4]. There the absolute normalization of the code was provided by a mock beam stop experiment[8], LAMPF experiment E866. Error estimates for the present KARMEN experiment are given in Table 5. The measured pion production cross sections used

in the Monte Carlo code typically have 9.5% absolute normalization errors. However, because the code was instead normalized to the E866 data on stopped π^+ per incident proton, this 9.5% uncertainty is irrelevant and is not included.

The sensitivity to the modelling of the geometry of the pressure vessel was investigated by changing the distribution of iron and water within the pressure vessel, but without changing the mass of these components. This produced an effect of 0.4%. No changes to the uranium disks were necessary as the geometry of these was modelled exactly.

The sensitivity to the beam geometry was investigated by displacing the beam by 1 cm in the horizontal and vertical planes. If a significant fraction of the beam intensity were to be so displaced, (either because of beam wander or the presence of a significant beam halo) the ISIS beam diagnostics would cause the beam to trip off. Similarly, the beam may be wider or narrower than the nominal 70mm diameter. These changes increase or decrease the neutrino production respectively. However, the effects are not independent; if the beam is narrower then the probability of beam wander (or halo) changing the neutrino production is reduced. It is unlikely that the beam spot could be narrower than 50mm as the temperature rise of the uranium target would cause the beam to trip off. The largest change in the neutrino production found was 0.6%, and this was adopted as the error due to uncertainties in the beam geometry.

The main difference between the π^+ decay-at-rest and the μ^- decay-at-rest uncertainties in Table 5 occur in the absolute normalization. A normalization uncertainty for π^- decay in flight is composed of both a 9.5% contribution from the absolute normalization errors quoted in the pion production measurements, and a 5.0% contribution from the E866 experiment. This latter number comes from the part of the "systematic effects in E866" entry in Table 2 that represents a change in the code normalization, but that does not involve the pion production cross section errors.

In addition, a larger number (5.0%) is used for the ISIS simulation uncertainty in the π^- decay-in-flight flux. The number of pions that can decay in flight are quite sensitive to the open spaces between spallation target components. The elements of the target in-line with the proton beam are quite well defined, but the moderator and shielding surrounding the target are not so well described. Therefore, computer runs were made with movements of various of the shielding components. Typically, for a movement of 2.5 cm, the decay-in-flight flux changed up to 8%. A reasonable estimate for the likely flux uncertainty from the open space uncertainty is 5% and is the entry in Table 8.

7 Summary

A Monte Carlo computer code for calculation of neutrino fluxes from the ISIS neutron spallation facilty has been described with particular emphasis on inclusion of π^- production and transport. The simulation of the spallation and μSR targets at the ISIS facility, needed for geometry input to the code, was described in some detail. Application of the code, for ν_μ, ν_e, and $\overline{\nu}_\mu$ fluxes resulting from π^+ and μ^+ decay at rest, were presented for

Table 6: Estimated errors in the calculated neutrino fluxes from π^+ decay at rest and μ^- decay at rest.

Source of uncertainty	π^+ Decay at rest (%)	μ^- Decay at rest (%)
Fit of E866 data	2.4	-
Cross section error	-	9.5
Systematic effects in E866	5.9	5.0
ISIS simulation	0.4	5.0
Proton beam energy	0.3	0.3
Protons on target	2.0	2.0
Proton geometry	0.6	0.6
Quadrature sum	6.7	12.0

both tantalum and uranium spallation targets and a pyrolytic graphite μSR target, and for incident proton beams of 750 and 800 MeV. An absolute accuracy of 6.7% on these neutrino fluxes was calculated from the normalization to a mock beam stop experiment.

The $\overline{\nu}_e$ backgrounds from the π^- decay-in-flight and subsequent μ^- decay-at-rest chain were also listed for the same target and proton beam combinations. The accuracy of these calculations was estimated to be 12% from a combination of the mock beam stop experiment and the uncertainties in the measured pion production cross sections. Use of the time structure of the proton beam at ISIS can reduce this background to a value $\overline{\nu}_e / \nu_e = 0.6 \times 10^{-3}$.

8 Acknowledgements

We wish to acknowledge helpful conversations with T. Broome, G. H. Eaton, and M. Holding. We are grateful to M. Albert and D. Works for testing the Monte Carlo code, and to the former for the subroutine that calculated decay-in-flight absolute fluxes. This work was supported in part by the Forschungszentrum Karlsruhe (Germany), by the Department of Energy (USA), and by the Engineering and Physical Sciences Research Council (UK).

A Cross section algorithms

In order to make this discussion self-contained, we reproduce here, from Sec. 4.2, the simple algorithmic form of eq. (1) for the doubly-differential π^- production cross section. The dependence upon π^- energy T_π, for a given material Z and proton kinetic energy T_p, is:

$$\frac{d^2\sigma}{d\Omega_\pi dT_\pi} = \left[A_1 e^{-\left(\frac{\overline{T}-T_\pi}{\sqrt{2}\sigma_1}\right)^2} + A_2 e^{-\left(\frac{T_\pi}{\sqrt{2}\sigma_2}\right)^2} \right] \times \left(1 + e^{\frac{T_\pi - T_F}{B}}\right)^{-1}. \qquad \text{(A.1)}$$

The functional forms of the parameters $A_{1,2}$, $\overline{T}$and $\sigma_{1,2}$ appearing in eq. (1) were fit, to data in references[10, 12], with a combination of piecewise-continuous linear functions and simple exponentials. Although seemingly more awkward than a generalized fit to, *e.g.*, n^{th}-order polynomials, these constructed forms have the very important properties that (a) a minimum of coefficients, sufficient for the accuracies needed in this Monte Carlo calculation, are introduced, and (b) the functional forms vary quite smoothly for interpolations and extrapolations in proton energy T_p and atomic number Z. Standard minimization techniques were used, but weighting all points equally, to fit to the data at the two proton energies $T_p = 585$ and 730MeV for carbon, aluminum, copper and lead.

The parameters $\sigma_{1,2}$ are found to be essentially independent of the atomic number Z:

$$\begin{aligned} \sigma_1(\theta, T_p) &= e^{-\left(\frac{\theta}{89}\right)} \left(-150(T_p - 730) + 162(T_p - 585)\right)/(730 - 585) \qquad \text{(A.2)} \\ \sigma_2(T_p) &= 30, \qquad T_p > 650\text{MeV} \\ &= 55, \qquad T_p \leq 650\text{MeV}, \end{aligned}$$

where θ is measured in degrees.

Two ranges in Z enable the centroid position of the first Gaussian term in eq. (A.1), $\overline{T}(\theta,T_p,Z)$, to have its θ dependence parameterized in a simple exponential form, and its T_p dependence in a similar form:

$$\begin{aligned} \overline{T}(\theta, T_p, Z) &= 32.3 + 205e^{-\left(\frac{\theta}{TA}\right)} \qquad \text{(A.3)} \\ TA &= \left(-39.6(T_p - 730) + 44.2(T_p - 585)\right)/(730 - 585), \qquad Z \leq 12 \\ &= \left(-20.7(T_p - 730) + 25.4(T_p - 585)\right)/(730 - 585), \qquad Z > 12 \end{aligned}$$

Here, TA is taken to be a linear function of T_p, interpolated between measured values at 730 and 585 MeV. and extrapolated linearly above 730 MeV and below 585 MeV with the same slope.

The dependence upon atomic number, Z, of the amplitudes $A_{1,2}$ is most easily handled by defining the amplitudes for two step-wise ranges in Z: $Z \leq 12$, and $Z > 12$. For the amplitude A_1, we find a linear dependence upon θ for the lower range in Z, while in

Table A.1: T_p and θ dependence for the coefficients c_i.

Coefficient	$T_p \leq 650$ MeV		$T_p > 650$ MeV	
	$\theta < 60^o$	$\theta \geq 60^o$	$\theta < 45^o$	$\theta \geq 45^o$
c_1	4.40	2.89	6.15	3.86
c_2	.023	.0019	.055	.0041
c_3	11.24		13.20	

the upper range there is a further depence upon neutron number, $N = A - Z$, but no dependence upon angle:

$$\begin{aligned} A_1 &= c_1 - c_2\theta, & Z \leq 12 \\ A_1 &= c_3\sqrt{N/34.5}, & Z > 12 \end{aligned} \tag{A.4}$$

The values of the coefficients c_i for appropriate ranges in T_p and in θ are given in Table A.1 . For the amplitude A_2, the value in the lower range of Z is zero, while the value in the higher range of Z is given by a more complicated expression:

$$\begin{aligned} A_2 &= 0.0, & Z \leq 12 \\ A_2 &= f(\theta, N, T_p)(d_7 + d_8)\sqrt{N}, & Z > 12 \end{aligned} \tag{A.5}$$

To compute $f(\theta, N, T_p)$ it is convenient to separate the N and θ dependence by first introducing the parameterization

$$\begin{aligned} X_a &= d_1 + d_2\left(1 - e^{-N/d_3}\right) \\ X_b &= d_4 + d_5 e^{-N/d_6} \end{aligned} \tag{A.6}$$

where the coefficients $d_{1,\ldots,8}$ in eqs. (A.5-A.6), are listed in Table A.2 for two ranges of T_p. Then the factors X_a, X_b are combined to form the terms $f(\theta, N, T_p)$ for first the energy range $T_p \leq 650$ MeV:

$$\begin{aligned} f(\theta, N, T_p) &= 1. + X_a\theta, & \theta < 60^o \\ &= 1. + 60(X_a - X_b) + X_a\theta, & \theta \geq 60^o \end{aligned} \tag{A.7}$$

and then the energy range $T_p > 650$ MeV:

$$\begin{aligned} f(\theta, N, T_p) &= 1. + X_a\theta, & \theta < 45^o \\ &= 1. + 45(X_a - X_b) + X_a\theta. & \theta \geq 45^o \end{aligned} \tag{A.8}$$

After the doubly-differential π^- production cross sections are defined, they are normalized in the Monte Carlo code to the measured total cross sections as described in Sec. 4.2 .

Table A.2: T_p and dependence for the coefficients d_i.

Coefficient	$T_p \leq 650$ MeV	$T_p > 650$ MeV
d_1	-0.2690	-0.1123
d_2	0.2621	0.1043
d_3	8.	12.
d_4	0.0040	0.00021
d_5	0.4473	0.00576
d_6	5.	10.
d_7	-11.36	3.21
d_8	-13.33	4.44

References

[1] B. Boardman, Rutherford Laboratory report, RL-82-006 (1982).

[2] B. Armbruster, *et al.*, Nucl. Phys. **B** (Proc. Suppl.) **38** (1995) 198; B. Armbruster, *et al.*, Nucl. Phys. **B** (Proc. Suppl.) **38** (1995) 235.

[3] T.A. Gabriel, *et al.*, Kernforschungszentrum Karlsruhe report, KfK 3174 (1981).

[4] R.L. Burman, M.E. Potter and E.S. Smith, Nucl. Instr. and Methods **A291** (1990) 621.

[5] I.S.K. Gardner, private communication.

[6] G.H. Eaton *et al.*, Nucl. Instr. and Meth. A269 (1988) 483.

[7] J.F. Breismeister, Editor, "MCNP - A general Monte Carlo code for neutron and photon transport," Los Alamos National Laboratory manual LA-7396-M, Rev. 2 (1986)

[8] R.C. Allen, *et al.*, Nucl. Instr. and Methods **A284** (1989) 347.

[9] D. Ashery *et al.*, Phys. Rev. C23 (1981) 2173.

[10] D.R.F. Cochran *et al.*, Phys. Rev. D6 (1972) 3085.

[11] T. Suzuki, D.F. Measday and J.P. Roalsvig, Phys. Rev. C35 (1987) 2212.

[12] J.F. Crawford *et al.*, Phys. Rev. C22, (1980) 1184.

[13] R.L. Burman and E.S. Smith, Los Alamos National Laboratory report, LA-11502-MS (1989)

[14] T.W. Dombeck, Los Alamos National Laboratory report LA-UR 82-1589 (1982).

[15] D. Ashery and J.P. Schiffer, Ann. Rev. Nucl. Part. Sci. **36** (1986) 207.

[16] S. Wölfle, private communication.